Stress and deformation induced in layered media by cylindrical thermo-poro-elastic sources: An application to Campi Flegrei (Italy)

Published Version:
Nespoli, M., Belardinelli, M.E., Bonafede, M. (2021). Stress and deformation induced in layered media by cylindrical thermo-poro-elastic sources: An application to Campi Flegrei (Italy). JOURNAL OF VOLCANOLOGY AND GEOTHERMAL RESEARCH, 415, 1-14 [10.1016/j.jvolgeores.2021.107269].

Availability:
This version is available at: https://hdl.handle.net/11585/820130 since: 2021-05-20

Published:
DOI: http://doi.org/10.1016/j.jvolgeores.2021.107269

Stress and deformation induced in layered media by cylindrical thermo-poro-elastic sources: an application to Campi Flegrei (Italy)

Massimo Nespoli[a], Maria Elina Belardinelli[a], Maurizio Bonafede[a]

[a] *Department of Physics and Astronomy, Alma Mater Studiorum, University of Bologna, Bologna, Italy*

Abstract

In recent literature thermo-poro-elastic (TPE) inclusions are proposed to contribute to deformation and stress in volcanic and hydrothermal areas. With respect to previous works, the present study implements the modeling improvements requested for a more realistic description of a TPE source and the embedding medium. Firstly we propose a numerical method to represent inclusions with an arbitrary geometry. In the case of cylindrical-shaped sources, the proposed approach allows us to study the effects of the source thickness on both deformation and stress fields. Moreover, we are allowed to consider depth dependent pore pressure and temperature changes within the inclusion, as expected during the transient stage of hot fluid propagation. Secondly, we take into account elastic stratification of the crust, in order to perform unbiased inversion of ground deformation data. The inversion of geodetic data collected during the 1982-84 unrest episode in the Campi Flegrei caldera (Italy), performed in a layered elastic medium, leads to a lower misfit and a deeper deformation source with respect to the one obtained inverting data in a homogeneous half-space. Furthermore, the geometry and location of the thermo-poro-elastic inclusion retrieved from the inversion in the layered medium leads to a shear stress distribution in good agreement with the relocated seismicity observed at Campi Flegrei. Most hypocenters are found to be located near and inside the TPE inclusion boundaries, where the greater shear stress is predicted. With respect to previous works we also found that vertical gradients of pore pressure and temperature and elastic layering can promote both normal and thrust earthquakes within the inclusion.

Keywords: Temperature, Pore pressure, TPE source thickness, Layered structure, Inversion, Campi Flegrei

1. Introduction

The ground deformation in volcanic regions can be ascribed to both hydrothermal fluid circulations and inflation/deflation of a magmatic body (*e.g.* Rinaldi et al., 2010; Macedonio et al., 2014; Lima et al., 2009). In the literature there are several representations of deformation sources which consider different geometries and arise from conceptually different physical models. Spherical and spheroid magma filled, pressurized cavities (*e.g.* Yang et al., 1988; Mogi, 1958; McTigue, 1987) are well suited to represent magmatic reservoirs (i.e. magma chambers) in elastic half-spaces and several works confirm their ability to represent deformations and gravity changes in volcanic environments (*e.g.* Bonafede and Ferrari, 2009; Berrino et al., 1984; McKee et al., 1989). Differently, sill-like magma intrusions and dikes can be modeled in terms of tensile dislocations (Okada, 1992, 1985) or circular cracks (Fialko et al., 2001). In addition to these, there is another kind of physical model which attribute the surface deformation to a Thermo-Poro-Elastic (TPE) inclusion (Belardinelli et al., 2019; Mantiloni et al., 2020). The deformations induced by the TPE inclusions are due to the mechanical effects of both pore pressure and temperature changes of the fluids which pervade a poroelastic region with assigned geometry (the TPE inclusion), embedded in an elastic medium (the matrix). With respect to the other models, the TPE inclusions are suitable to represent volcanic environments in which there is no evidence of a shallow magmatic body, as it is for the nested caldera of Campi Flegrei in Italy (Judenherc and Zollo, 2004). In fact, they can justify deformations of the same order of magnitude as other models resembling magma chambers, but assuming fluid related thermo-poro-elastic effects. At Campi Flegrei, De Siena et al. (2010) evidenced the presence of shallow gas reservoirs. The tomography performed by Calò and Tramelli (2018) sustains the existence of a seismic layer which separates the shallow aquifer from the deeper part of the caldera. This structure must have an important role in regulating the ascent of fluids from the deeper magma chamber to the surface as it can both prevents the ascent of fluids coming from below or releases them, owing to a time dependent permeability. Before the occurrence of the unrest phase started in 1982 at Campi Flegrei, this structure acted as a barrier to the fluid flow, due to its low permeability. During the unrest, the stress increase induced by the deep magmatic source fractured the layer, allowing for the fluid diffusion within it (Calò and Tramelli, 2018). The pore pressure increase likely triggered a cascade mechanism that led to a strong fracturing of such structure and a consequent increase of its permeability.

Within this conceptual model, the TPE inclusion both represents the mentioned structure and a source of deformation through its thermo-poro-elastic effects (Figure 1).

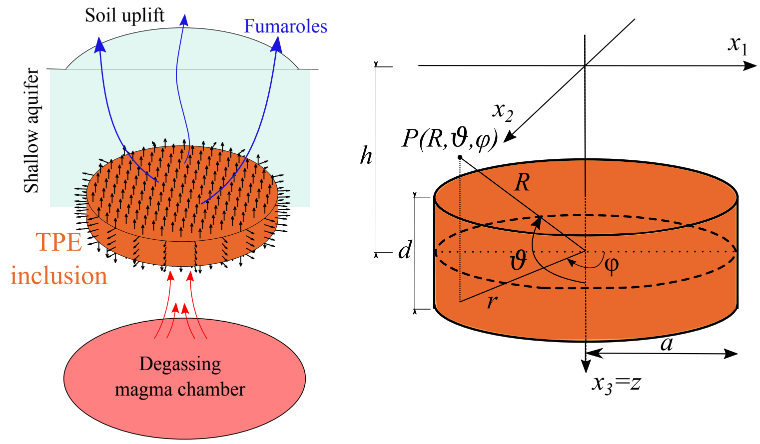

Figure 1: Conceptual model of a disk shaped TPE inclusion (orange) placed above a degassing magma chamber (red). Due to the injection of hot and pressurized fluids from the parent magma chamber, the TPE inclusion exerts a mechanical effect on the surrounding medium (*e.g.* a surface aquifer). The black arrows schematically represent single forces distributed on the surface of the disk shaped TPE inclusion placed at a depth h, with a thickness d, and a radius a.

In literature semi-analytical approaches were proposed to model the effects of TPE inclusions with simple geometries. Stress and displacement induced by spherical and spherical-shell TPE inclusions were obtained by Belardinelli et al. (2019) in a homogeneous full-space. Despite the simple geometry of the model, Belardinelli et al. (2019) found that a spherical shell TPE inclusion can induce significant deviatoric stress by reasonable increments of pore pressure and temperature. They also found that a compressive environment is generated inside the inclusion, while an extensional environment is generated outside it. Accordingly, this kind of source can predict the heterogeneity of focal mechanisms often observed in the seismicity induced by volcanic activity (*e.g.* D'Auria et al., 2011; Ekstrom, 1994). The more recent model by Mantiloni et al. (2020) represents thin-disk TPE inclusions embedded in a homogeneous half-space. With respect to TPE inclusions with a spherical-shell geometry, a disk-shaped geometry can better represent horizontal and permeable rock layers stressed and strained by hot and pressurized volatiles. Furthermore, thanks to the modeling of the free surface, Mantiloni et al. (2020) were able to compare their model predictions with surface displacement measured during the 1982-1984 unrest episode at the Campi Flegrei caldera (Italy). For this episode, they found that a disk-shaped TPE source leads to a lower misfit with the data than spherical pressurized sources and circular cracks. In volcanic regions, the effects of other sources of deformation such as faults and dikes (*e.g.* Gudmundsson, 2020) can be expected in addition to the ones due to a TPE inclusion, to which the present paper is restricted.

In this work we aim to further improve the modeling of TPE inclusions by accounting for an arbitrary geometry, non-uniform pore pressure and temperature inside them and the stratication of the elastic embedding medium. The second improvement is necessary to represent the expected distributions of pore pressure and temperature changes realized at a specific state of the transient fluid propagation and temperature diffusion within a TPE inclusion, as we will show herein.

2. The model

The deformation and stress field of the TPE sources can be obtained analytically in a full space (Belardinelli et al., 2019), while a semi-analytical computation is required in the case of a half-space (Mantiloni et al., 2020). The computation is performed according to the Eshelby (1957) approach. For a thermo-poro-elastic medium, the constitutive relations giving the strain tensor e_{ij} in terms of the stress tensor τ_{ij}, can be written following McTigue (1986) as

$$e_{ij} = \frac{1}{2\mu}\left(\tau_{ij} - \frac{\nu}{1+\nu}\tau_{kk}\delta_{ij}\right) + \frac{1}{3H}p\delta_{ij} + \frac{1}{3}\alpha_s T\delta_{ij} \tag{1}$$

where, μ is the rigidity, H is the Biot's constant, α_s the thermal expansion coefficient of the solid matrix, ν the drained isothermal Poisson's ratio; T and p are temperature and pore pressure changes from a reference equilibrium configuration (in the following we shall assume an isothermal configuration in hydrostatic equilibrium). The last two terms in the second member of the previous equation represent the so called stress-free strain $e^*_{ij} = e_0\delta_{ij}$ (Eshelby, 1957; Aki and Richards, 2002; Backus and Mulcahy, 1976), where

$$e_0 = \frac{1}{3H}p + \frac{1}{3}\alpha_s T \tag{2}$$

represents the isotropic strain change that the inclusion (*i.e.* the region with $T \neq 0$ and $p \neq 0$) would undergo if extracted from the elastic embedding matrix (*e.g.* Belardinelli et al., 2019). The quantity e_0 linearly depends on the pore pressure and temperature changes of the fluids inside the inclusion. Its importance stems from the fact that e_0 determines the magnitude of all the mechanical effects of the TPE inclusion as a deformation source. Accordingly, in the following e_0 will be referred as *"TPE inclusion potency"*. The poroelastic parameter $1/H$ is related to the drained isothermal bulk modulus of the medium $K = \frac{2\mu(1+\nu)}{3(1-2\nu)}$ and the unjacketed bulk modulus K'_s, through the relation $1/H = 1/K - 1/K'_s$.

In order to keep constant the volume of the inclusion after the occurrence of temperature and pore pressure changes, tractions $T_k = -3Ke_0n_k$ must be applied over its surface, where a discontinuity of tractions

$[T_k]_-^+ = 3Ke_0 n_k$ arises (Belardinelli et al., 2019; Mantiloni et al., 2020). The continuity of tractions across the TPE inclusion surface S is assured (Aki and Richards, 2002) when an equilibrium between the inclusion and the embedding medium is reached (assuming drained and isothermal conditions). At this stage the displacement produced by the TPE inclusion is expressed as

$$u_i(\mathbf{x}) = \oint_S G_{ik}(\mathbf{x},\mathbf{x}')\,[T_k]_-^+\,dS' = \oint_S 3Ke_0 G_{ik}(\mathbf{x},\mathbf{x}')n_k(\mathbf{x}')dS', \tag{3}$$

where the Green's tensor component $G_{ik}(\mathbf{x},\mathbf{x}')$ represents the $i-th$ component of the displacement in $\mathbf{x}$ due to a single, unitary point force located in $\mathbf{x}'$, with the $k-th$ direction. In the case of single forces placed in the interior of a uniform elastic half-space, the G_{ik} components are provided by Mindlin (1936). It is worth noting that equation (3), which includes a surface integral, is sufficient to compute displacements in each point of the half-space (i.e. both inside and outside the TPE inclusion). Nevertheless, in order to perform analytical or semi-analytical integrations, previous authors (Belardinelli et al., 2019; Mantiloni et al., 2020) proceeded with an equivalent integration over the volume of the TPE inclusion, V_S, which can be obtained by applying the Gauss' theorem to eq. 3,

$$u_i(\mathbf{x}) = \int_{V_S} 3Ke_0 \frac{\partial G_{ik}}{\partial x'_k}(\mathbf{x},\mathbf{x}')dv(\mathbf{x}') \tag{4}$$

Once the displacement has been computed, we can compute the strain e_{ij} and the stress τ_{ij} field inside (in) and outside (out) the inclusion as

$$e_{ij} = e_{ij}^{in} = e_{ij}^{out} = \frac{1}{2}\left(\frac{\partial u_i}{\partial x_j} + \frac{\partial u_j}{\partial x_i}\right) \tag{5}$$

$$\tau_{ij}(\mathbf{x}) = \tau_{ij}^{in} = \lambda e_{kk}\delta_{ij} + 2\mu e_{ij} - 3Ke_0\delta_{ij},\ \mathbf{x} \in V_S \tag{6}$$

$$\tau_{ij}(\mathbf{x}) = \tau_{ij}^{out} = \lambda e_{kk}\delta_{ij} + 2\mu e_{ij},\ \mathbf{x} \notin V_S \tag{7}$$

2.1. Pore pressure and temperature distribution inside the TPE source

According to the conceptual model of Figure 1, the TPE inclusion potency depends on the temperature and pressure variations of hot and pressurized fluids exolved from a deeper reservoir and rising within the TPE source region. The TPE inclusion potency, e_0 can be treated as an independent term and in this subsection we provide some hint to the depth dependence of both p and T, at a given instant of time, t, assuming plausible boundary conditions, following the entrance, at $t = 0$, of hot and pressurized fluids at the bottom ($z = h + d/2$) of the TPE inclusion. To describe the space-time evolution of p and T two basic equations should be solved with parameters of both fluid and solid phases reported in Table 1. The fluid phase has a density ρ_f, conductivity λ_f, specific heat c_f and viscosity η. The solid matrix has porosity ϕ, density ρ_s, specific heat c_s and thermal conductivity λ_s. The permeability of the medium is k (see Table 1).

The first basic equation states the energy balance of the system (*e.g.* Bejan, 1984; Zencher et al., 2006)

$$\rho c \frac{\partial T}{\partial t} + \rho_f c_f \mathbf{q} \cdot \nabla T = \lambda \nabla^2 T - \mathbf{q} \cdot \nabla p \tag{8}$$

where $\mathbf{q} = (k/\eta)\nabla p$ is the fluid discharge rate, while $\rho c = \phi \rho_f c_f + (1-\phi)\rho_s c_s$ and $\lambda = (1-\phi)\lambda_s + \phi \lambda_f$ denote average specific heat per unit volume and average conductivity, respectively. The second equation can be derived from the fluid mass conservation (*e.g.* McTigue, 1986)

$$\left[\frac{\partial}{\partial t} - D\nabla^2\right]\left(\tau_{kk} + \frac{3}{B}p\right) = D\beta_1 \nabla^2 T + \beta_2 \frac{\partial T}{\partial t}, \quad \beta_1 = \mu \alpha_s \frac{4}{3}\frac{1+\nu}{1-\nu}, \quad \beta_2 = 2\mu B \phi (\alpha_f - \alpha_s)\frac{(1+\nu)(1+\nu_u)}{3(\nu_u - \nu)} \tag{9}$$

where B is the Skempton parameter describing $p = -B\tau_{kk}/3$ in undrained conditions (e.g., Nespoli et al., 2018), ν_u is the undrained Poisson ratio, α_s and α_f are thermal expansion coefficients for the solid and fluid phase, respectively, and D is the hydraulic diffusivity

$$D = \frac{k\mu}{\eta}\frac{2B^2(1+\nu_u)^2(1-\nu)}{9(1-\nu_u)(\nu_u - \nu)}$$

In equation 9 the term multiplied by β_1 describes purely thermo-elastic effects, while the term multiplied by β_2 describes the fluid pressure that would be induced in undrained conditions by the greater (typically)

Table 1: Material parameters for Berea sandstone saturated with liquid water (Rice and Cleary, 1976). Density ρ_s, ρ_f in [kg/m^3], specific heath c_s, c_f in [J/(kg K)], permeability k in [m^2], thermal conductivity λ_s, λ_f in [W/(m K)], rigidity μ in [Pa], thermal expansion α_s, α_f in [K^{-1}], fluid viscosity η in [Pa s], hydraulic diffusivity D in [m^2/s], bulk modulus of solid $K_s \sim K'_s$ in [Pa]. Porosity ϕ, Poisson ratios ν, ν_u and Skempton parameter B are non-dimensional. The subscripts f and s refer to the fluid phase and to the solid phase of the poro-elastic medium, respectively.

Rock properties (measured)								
ρ_s	c_s	ϕ	k	λ_s	μ	ν	K_s	α_s
2650	10^3	0.19	$1.9 \cdot 10^{-13}$	2.5	$6 \cdot 10^9$	0.2	$36 \cdot 10^9$	$3 \cdot 10^{-5}$
Fluid properties					**TPE properties**			
ρ_f	c_f	η	λ_f	α_f	H	B	ν_u	D
1000	4200	10^{-3}	0.6	$5 \cdot 10^{-4}$	$10.1 \cdot 10^9$	0.62	0.33	1.6

Table 2: TPE inclusion potency, e_0 as function of different p and T values, employing parameters for Berea sandstone (Table 1).

TPE inclusion potency $e_0(p,T)\cdot 10^{-3}$						
$T(K)$ / $p(\cdot 10^7 Pa)$	0	100	200	300	400	500
0	0.00	1.00	2.00	3.00	4.00	5.00
0.5	0.17	1.17	2.17	3.17	4.17	5.17
1.0	0.33	1.33	2.33	3.33	4.33	5.33
1.5	0.50	1.50	2.50	3.50	4.50	5.50
2.0	0.66	1.66	2.66	3.66	4.66	5.66
2.5	0.83	1.83	2.83	3.83	4.83	5.83
3.0	0.99	1.99	2.99	3.99	4.99	5.99

thermal expansion of the fluid enclosed within pore spaces.

2.1.1. High permeability approximation

Equations 8 and 9 may be substantially simplified considering a high permeability ($1.9\cdot 10^{-13}$ m^2, Table 1) and low thermal conductivity medium with small thickness d. Permeability values retrieved by experimental measurements and drillings at Campi Flegrei ranges from $\sim 10^{-17}$ to $\sim 10^{-13}$ m^2 (Todesco et al., 2010), so in this paragraph we assume a permeability value pertinent to an upper bound for Campi Flegrei. Volatiles exsolved from a magmatic reservoir are typically released at near-lithostatic pressure and at temperatures in the order of 10^3 K (*e.g.* Parfitt and Wilson, 2008). Assuming the bottom of the TPE inclusion located at a depth $z = 3$ km, the lithostatic pressure in excess of hydrostatic may be evaluated as $p \sim 4 \div 5\cdot 10^7$ Pa. However the fracture toughness of volcanic rocks is generally estimated of the order of some MPa. Accordingly, at the bottom of the TPE inclusion, $\Delta T \sim 500$ K and $\Delta p \sim 10^7$ Pa are upper values for the increments of temperature and pore pressure. Then, for parameters pertinent to a high permeability sandstone saturated with liquid water at 350 K (Table 1), the value of the TPE inclusion potency at its bottom is $\Delta e_0 \sim 0.005$ (Table 2). In this case, both the dissipative heat production $\mathbf{q}\cdot\nabla p$ and thermal conduction $\lambda\nabla^2 T$ in the r.h.s. of (8) can be neglected. We assume an initial homogeneous temperature field in $h - d/2 \le z \le h + d/2$ and $\mathbf{q}$ as slowly variable. Imposing $T = 0$ as initial condition (before exsolved fluids start flowing in $h - d/2 \le z \le h + d/2$) and $T = \Delta T$ as boundary condition in $z = h + d/2$, we obtain the simple solution expressed in terms of the vertical coordinate $\zeta = h + d/2 - z$ increasing upward (Figure 2 a):

$$T(\zeta,t) = \Delta T\left[1 - \Theta(\zeta - V_T t)\right] \tag{10}$$

where Θ is the Heaviside's step function and $V_T = \frac{\rho_f c_f}{\rho c} q \sim 5.4 \cdot 10^{-6}$ m/s is the speed of the temperature front (rising upwards) which reaches the top of the TPE layer $\zeta = d = 500$ m at $t = t_T = d/V_T = 9.3 \cdot 10^7$ s ($\sim$ 3 years). Due to the large value of D (for parameters of Table 1), the characteristic diffusion time for pore pressure is less than 2 days ($t_p = d^2/D = 5.7 \cdot 10^4$ s, from 9).

According to Wang (2017), in a poro-elastic context p is mathematically uncoupled from τ_{kk} in four circumstances: *i*) steady state; *ii*) uniaxial strain and constant vertical stress; *ii*) a highly compressible fluid; *iv*) an irrotational displacement field in an infinite or semi-finite domain without body forces. In order to grasp more clearly how the pore pressure evolves according to eq. (9), we may consider the simple 1-D (uniaxial strain and constant vertical stress) problem in which only $u_z \neq 0$ and u_z depends only on z, as it is turns out at least in the proximity of the symmetry axis of the TPE disk. In this case, $\tau_{xz} = \tau_{yz} = 0$, according to (6) and from the equilibrium equation ($\frac{\partial \tau_{ij}}{\partial x_j} = 0$), τ_{zz} must be constant. Expressing then $e_{zz} = e_{kk}$ from (1) in terms of τ_{zz}, τ_{kk} and e_0, one obtains $\tau_{kk} = (1+\nu)/(1-\nu)(\tau_{zz} - 4\mu e_0)$. This allows rewriting (9) for the pressure field alone in the following form

$$\left(\frac{\partial}{\partial t} - D\frac{\partial^2}{\partial \zeta^2}\right) p = \Sigma \frac{\partial T}{\partial t} \qquad \text{with} \quad \Sigma = (\beta_1 + \beta_2)\frac{B(1+\nu_u)(1-\nu)}{3(1+\nu_u)(1-\nu) - 6(\nu_u - \nu)}, \tag{11}$$

where only the time derivative of T remains in the thermal source term. It is worth to notice that the terms containing τ_{kk} in (9), in (11) has been expressed in terms of p and T. This equation may be solved using the technique of separation of variables imposing the boundary conditions: $p = \Delta p$ in $\zeta = 0$ and $p = 0$ in $\zeta = d$. The parameter Σ describes the pressure increment generated by a sudden unitary increase of temperature; it is strictly linked to the thermal expansion of the solid matrix and of the fluid, because cavities become larger and fluid expansion is constrained by the cavity volume. The solution of (11), employing the temperature field given by (10), shows that the pore pressure field rapidly attains (after a time span t_p) a profile with two constant gradients below and above the temperature front $\zeta = V_T t$; the two gradients are however very close to each other employing the mentioned parameter values, so that the flow rate $\mathbf{q}$ is nearly constant (Figure 2 c). It may be mentioned that the slightly greater volumetric flow rate above the temperature front is due to the expulsion of expanding heated water previously resident within porous cavities. Figure 2 shows that the TPE inclusion potency increases with depth. For $\Delta T = 500$ K the vertical profile of e_0 is step-like at the temperature front location $\zeta = V_T t$ (Figure 2*a*) while for a lower ΔT value e_0 tends to gets closer to the p profile (Figure 2*b*). For highly fractured rocks (for which $K \ll K_s$), the parameter $1/H$ (equation 2)

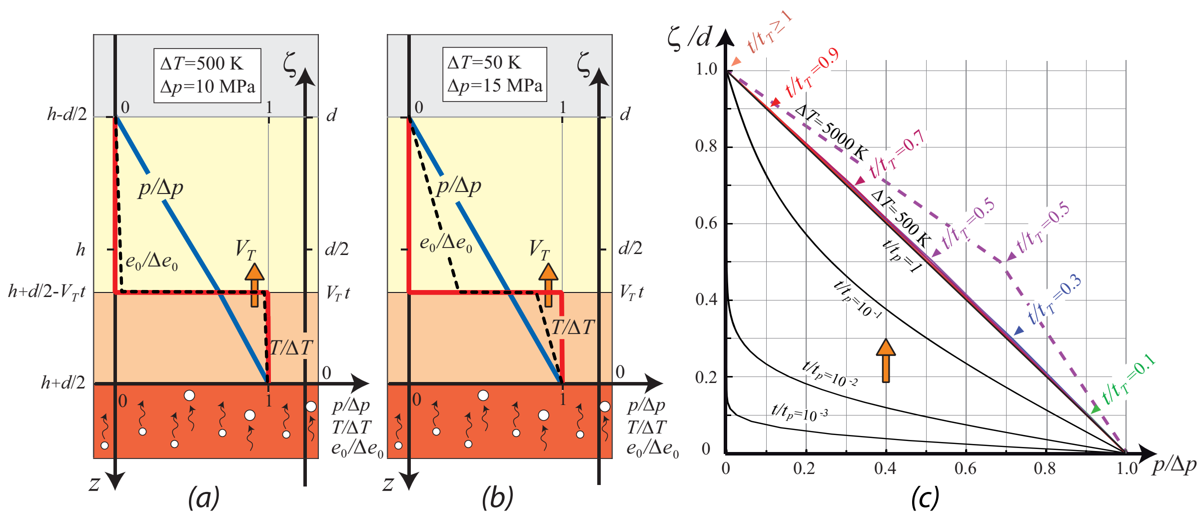

Figure 2: (a) Thermal advection front (red line), incremental pore pressure (blue) and TPE potency e_0 (black dashed line) in the TPE layer $h - \frac{d}{2} \leq z \leq h + \frac{d}{2}$, above a volatile-exsolving magma reservoir in $z > h + \frac{d}{2}$ (red box) at time $t = \frac{1}{3} t_T$. TPE-source thickness $d = 500\,\mathrm{m}$, boundary values: temperature increment $\Delta T = 500\,\mathrm{K}$, pore pressure increment $\Delta p = 10\,\mathrm{MPa}$, $\Delta e_0 = \frac{\Delta p}{3H} + \frac{\alpha_s \Delta T}{3} = 5.3 \times 10^{-3}$. (b) Same as in (a) assuming $\Delta T = 50\,\mathrm{K}$, $\Delta p = 15\,\mathrm{MPa}$, $\Delta e_0 = 10^{-3}$. (c) Evolution of the pressure front from $t = 0$ up to $t = t_T$ assuming boundary values as in (a). Pore pressure is practically insensitive to the thermal source in the short time range ($t \leq t_p$) (black lines) and even when $t > t_p$ as far as ΔT is reasonably high (coloured lines). Only for unrealistically high ΔT the thermal source becomes important, as shown by the dashed line drawn for $\Delta T = 5000\,\mathrm{K}$ at $t = 0.5 t_T$. Triangles denote the position of the thermal front in $\zeta = V_T t$ for a few values of t/t_T. Parameter values from table 4, pressure diffusion time $t_p = 5.7 \cdot 10^4$ s, thermal propagation time $t_T = 9.3 \cdot 10^7$ s.

and the permeability k can be much higher than those reported in Table 2, pertinent to Berea sandstone. Consequently, for assigned increases of pore pressure and temperature, also the TPE inclusion potency and the temperature front speed might be greater than reported above.

2.2. *The fully numerical approach*

Differently from previous works, in the present paper we employ a fully numerical procedure based on equation 3 as we will approximate the surface integral with a distribution of single forces over S (Figure 1), with a magnitude

$$F_n = 3 K e_0 \Delta S_n, \tag{12}$$

where ΔS_n represents the area of a portion of the discretized surface of the TPE inclusion ($\sum \Delta S_n = S$). This approach is numerically advantageous with respect to computing the displacement due to a distribution of three orthogonal force dipoles ($\frac{\partial G_{ik}}{\partial x'_k}$) over the volume of the inclusion V_S (equation 4), as the latter would require a finer spatial sampling and therefore a greater computation time. An even more important advantage is that the present method avoids introducing singularities within the TPE volume and thus allows computing displacement, stress and strain in the interior of the TPE volume as smooth functions of position.

Our numerical procedure is based on the EDGRN/EDCMP code (Wang et al., 2003) that we modified in order to include the representation of single point forces. Thanks to the fully numerical approach, with respect to Mantiloni et al. (2020) we are able to *i*) represent a thick disk (i.e. a cylinder) shaped TPE inclusion, as we do not need to impose the analytically convenient assumption of a thin inclusion; *ii*) take into account the vertical heterogeneities of the elastic parameters of the embedding medium. In this way we are able to produce a more realistic and versatile representation of the TPE inclusion, that we will apply for the inversion of surface deformation data of the 1982-1984 unrest episode at the Campi Flegrei caldera.

The EDGRN/EDCMP original code is based on numerical Green's function to compute elastic displacement and stress field generated by a dislocation in a layered half-space. The software consists in two different routines that must be executed separately. The first one, EDGRN, computes the Green's functions for point double-couples and dipoles in a layered half-space using the Hankel transform and the Thomson-Haskell propagator algorithm. The second one (EDCMP) computes the convolution integrations of the point sources to realize a dislocation with a finite surface. Using cylindrical coordinates, in the point $\mathbf{x} = (z, r, \theta)$, the displacement of the medium can be expressed by Hankel transform following Aki and Richards (2002) and Wang et al. (2003)

$$\mathbf{u}(z,r,\theta) \quad = \sum_m \int_0^\infty \left[U_m(z,\ell)\mathbf{Z}_\ell^m(r,\theta) + V_m(z,\ell)\mathbf{R}_\ell^m(r,\theta) + W_M(z,\ell)\mathbf{T}_\ell^m(r,\theta)\right] \ell d\ell, \tag{13}$$

$$0 \le \ell < \infty, \;\; m = 0, \;\; 1, \;\; 2$$

with U_m,V_m and W_m wavenumber, $\mathbf{Z}_\ell^m = \mathbf{e}_z Y_\ell^m(r,\theta)$, $\mathbf{R}_\ell^m = \left(\frac{\mathbf{e}_r}{\ell}\frac{\partial}{\partial r} + \frac{\mathbf{e}_\theta}{\ell r}\frac{\partial}{\partial \theta}\right) Y_\ell^m(r,\theta)$ and $\mathbf{T}_\ell^m = \left(\frac{\mathbf{e}_r}{\ell r}\frac{\partial}{\partial \theta} - \frac{\mathbf{e}_\theta}{\ell}\frac{\partial}{\partial r}\right) Y_\ell^m(r,\theta)$ surface vector harmonics, where the cylindrical surface harmonics, $Y_\ell^m(r,\theta)$, are expressed in terms of the Bessel functions of order m, $J_m(\ell r)$

$$Y_\ell^m(r,\theta) = J_m(\ell r) \begin{pmatrix} \cos(m\theta) \\ \\ \sin(m\theta) \end{pmatrix} \tag{14}$$

Depending on the degree of the harmonics m, the Hankel transforms give the solution for a point inflation ($m = 0$), a single force ($m = 0, 1$) or a double couple ($m = 0, 1, 2$). In order to represent a generic dislocation source, EDGRN computes three different point source types: CLVD (compensated linear vector dipole), dip-slip and strike-slip double couples. Accordingly, we modified the script to obtain Green's functions also for single forces. This was done computing the appropriate Bessel functions, according to Table 3 in Wang et al. (2003). The modified EDGRN routine was then set up in order to provide in output the Green functions for horizontal and vertical single forces f_x, f_y, f_z. We also modified the EDCMP routine in order to be able to *i*) read the new Green functions and *ii*) accept, as input variables, multiple single forces with pre-assigned moduli and 3D orientation.

To model the mechanical effects of the TPE inclusion, we firstly need to generate a suitable distribution of both Green functions and single forces (as *e.g.* in Figure 1). The distribution must be dense enough to avoid numerical instabilities but not too dense in order to limit the computation time. Analogously to the original version of EDGRN/EDCMP, which allows us to check that the numerical model is correctly set by comparing the solution obtained in a homogeneous half-space to the analytical solution in Okada (1992), we can compare the results of the modified version of the code to the analytical solutions provided by Mindlin (1936). Obviously, for the case of a thin TPE in a homogeneous half-space, we can compare the solution also with the one obtained semi-analytically by Mantiloni et al. (2020).

2.3. Modeling a thick TPE

We firstly study the effects of the thickness of the TPE inclusion. In Figure 3 we report the resulting stress field in the median plane ($z = h$, Figure 1) of three TPE inclusions with different thickness (d=200, 2000 and 4000 m, Table 3) and fixed radius (a=2000 m). The three configurations correspond to aspect ratios d/a=0.1, 1 and 2, thus only the geometry with the smaller thickness can be considered as a thin disk ($d/a << 1$). In this last case (Figure 3 a), the stress field obtained with the numerical computation is equivalent to the one computed semi-analytically. This is no more true in the case of a thick disk with $d/a = 1$ (Figure 3 b) as the semi-analytical solution incorrectly leads to a strongly different stress field, especially inside the TPE source ($r/a < 1$). This is due to the fact that in the semi-analytical computation the solution is developed using a scalar potential expanded in Legendre Polynomials under the assumption of a thin disk (eq. 12 in Mantiloni et al., 2020). Nevertheless, in a homogeneous medium this problem can be easily solved by representing the thick TPE disk as a superposition of thin TPE disks (Figure 3 c), as guaranteed by the unicity of the solution and the continuity of tractions over the TPE inclusion boundaries. The case of a very thick disk instead (d/a=2, Figure 3 d) cannot be easily accomplished in this way, due to the superposition of the discontinuities occurring at $R = \sqrt{x_1^2 + x_2^2 + (h-z)^2} = a$ generated by each sub-disk, which arise from the singular part of the stress tensor (see Mantiloni et al., 2020), even if the problem could be partially bypassed considering the analytic continuation (or interpolation) of solutions of each sub-disk. Accordingly, in Figure 3 d, only the results obtained with a distribution of Mindlin's single forces are shown for comparison. This ensures that the distribution of the numerical Green functions has been correctly implemented in the numerical code. It is worth to noting that in the case of a very thick TPE source, the stress field inside the inclusion is close to an isotropic state ($\tau_{rr} \simeq \tau_{\varphi\varphi} \simeq \tau_{zz}$).

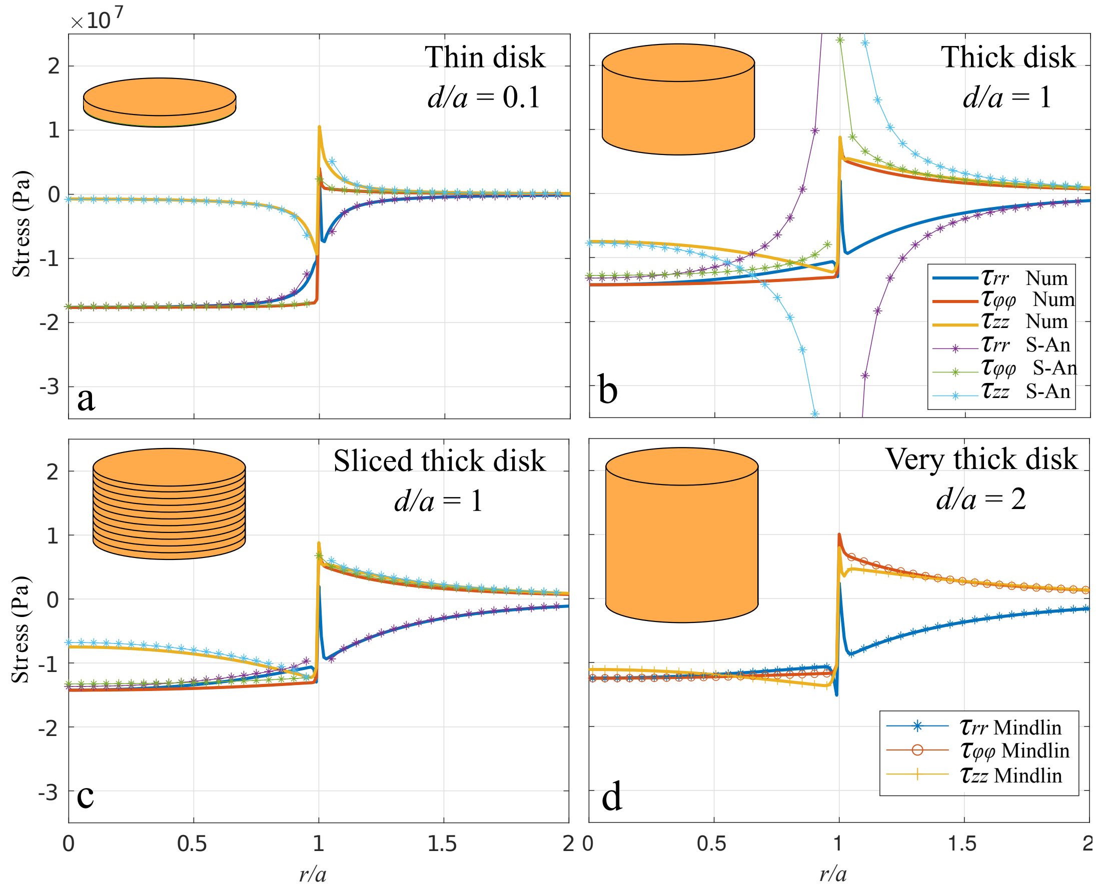

Figure 3: Comparison of the stress tensor computed numerically (Num) and semi-analytically (S-An) along the median plane ($z = h = 3000$ m) of three TPE inclusions with different thickness d=200 m (a), 2000 m (b) and 4000 m (d), fixed radius a=2000 m and $e_0 = 1 \cdot 10^{-3}$, $K = 8$ GPa, $\nu = 0.2$. In panel (c) the thick TPE inclusion (d/a=1) is represented as a superposition of 11 thin TPE disks. In panel d the solutions obtained with a distribution of single forces (using the Mindlin, 1936 solutions) are also shown.

In Figure 4 we show the comparison between the non-vanishing (not equal to zero) displacement components computed using the numerical model and the distribution of Mindlin's single forces for the three different aspect ratios (d/a). The results of both u_r and u_z components indicate that the magnitude of the displacement is strongly dependent on the thickness of the TPE inclusion as a thicker disk produces a greater displacement field.

Table 3: Parameters of the TPE inclusions of Section 2. Depth h =2 km, radius a =2 km and ν=0.2 for all cases.

Case	Figure	Thickness d (m)	$e_0 \cdot 10^{-3}$	K (GPa)
Thin disk	3a	200	1	8
Thick disk	3b	200	1	8
Sliced thick disk	3c	2000	1	8
Very thick disk	3d	4000	1	8
Uniform e_0	5a	2000	1	8
Variable e_0	5b	2000	1 ($0 < z \leq 2.5$ km) 2 ($2.5 < z \leq 3.5$ km) 3 ($z > 3.5$ km)	8
Elastic layering	5c	2000	1	8 ($0 < z \leq 2.5$ km) 16 ($2.5 < z \leq 3.5$ km) 24 ($z > 3.5$ km)

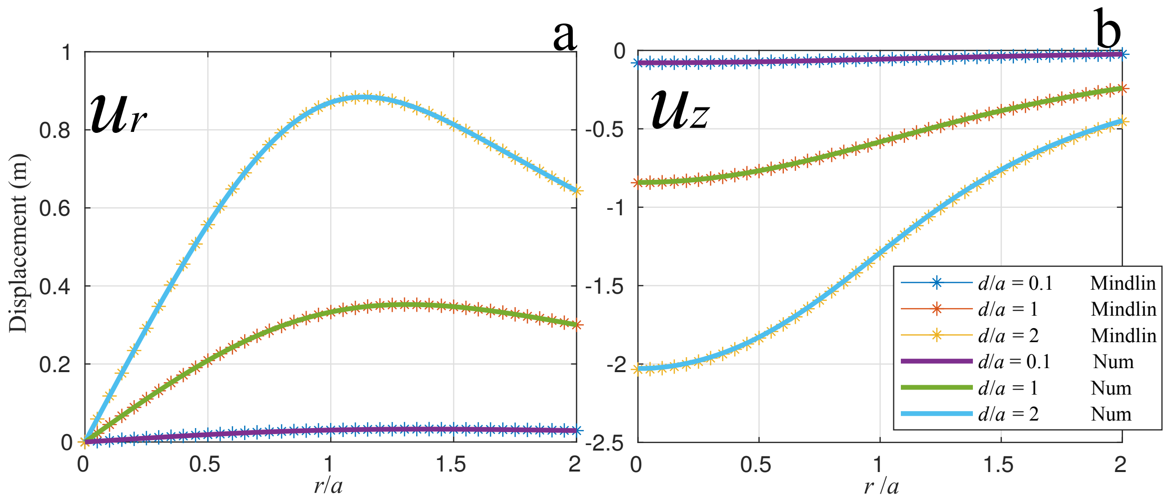

Figure 4: Comparison of displacement components u_r (a) and u_z (b) computed numerically (Num) and with a distribution of single forces (using the Mindlin, 1936 solutions) at the surface ($z = 0$) of three TPE inclusions with different thickness d=200 m (d/a=0.1), 2000 m (d/a=1) and 4000 m (d/a=2), fixed radius a=2000 m and $e_0 = 1 \cdot 10^{-3}$, $K = 8$ GPa, $\nu = 0.2$.

2.4. Modeling a non-uniform TPE inclusion

A non-uniform TPE inclusion potency, e_0, can derive from depth dependent changes of pore pressure p and/or temperature T as shown in section 2.1.1. Inside the TPE inclusion, a gradient of the potency e_0 along depth can be modeled using a superposition of stacked disks.

The comparison between the stress field generated by a uniform and a variable e_0 distribution of a thick TPE disk (a = 2000 m, h = 3000 m and d = 2000 m) is reported in Figure 5. The maximum shear stress distribution is also shown, to study how the TPE inclusion can induce seismicity. For the uniform case (Figure 5 a) we assume $e_0 = 10^{-3}$, while in Figure 5 b the thick TPE disk is discretized with three stacked disks of equal thickness, with depth-increasing e_0 ($1 \cdot 10^{-3}$, $2 \cdot 10^{-3}$, $3 \cdot 10^{-3}$). With respect to the uniform case, the maximum shear stress distribution induced by the TPE disk with variable e_0 attains the largest value near the bottom of the inclusion, while near the upper boundary the generated shear stress is even lower than the one computed in the uniform case. In both cases, according to Frohlich (2001), the

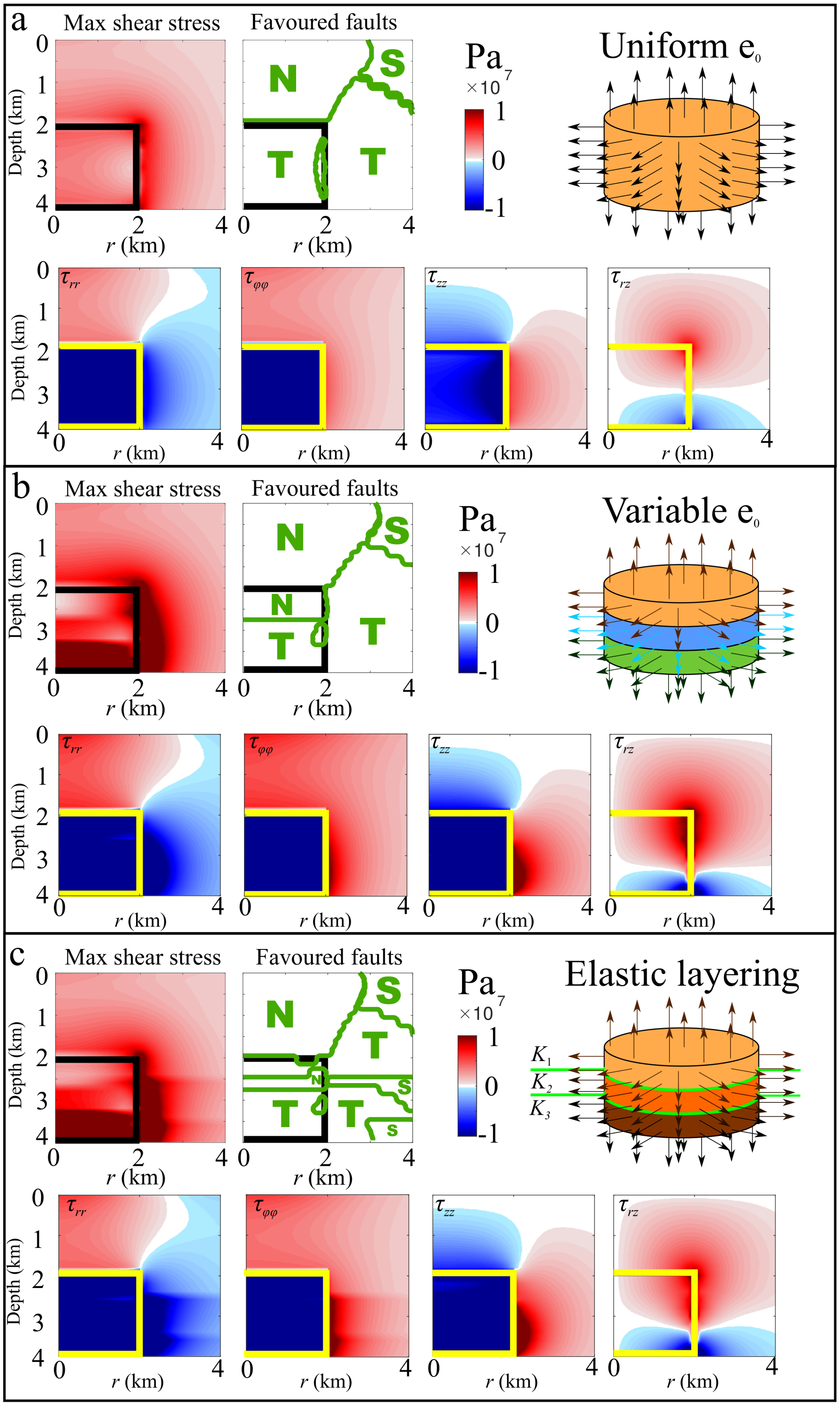

Figure 5: Maximum shear stress and stress components (Pa) in the case of a TPE inclusion with uniform potency $e_0 = 10^{-3}$ (a), a depth dependent potency e_0 (b). In both panels a and b the TPE source is located in a homogeneous half-space. In panel c we show the case of a TPE source located in a layered half-space with uniform e_0 potency, as in panel a. In panel a the TPE inclusion has $a = 2000$ m, $h = 3000$ m and $d = 2000$ m, while in panel b, the TPE is represented with 3 stacked disks with e_0 increasing with depth ($e_0 = 1 \cdot 10^{-3}$, $2 \cdot 10^{-3}$, $3 \cdot 10^{-3}$). In panel c the assumed values of the bulk modulus K are: $K_1 = 8$ GPa within the depth range 0-2500 m, $K_2 = 16$ GPa within the depth range 2500-3500 m and $K_3 = 24$ GPa below a depth of 3500 m. Black and yellow boxes represent the TPE inclusion boundaries, while green contours separates areas in which different earthquake mechanisms are favored (N=normal, S=strike-slip, T=thrust).

TPE sources promote thrust earthquakes in their interior (as found by Mantiloni et al., 2020), nevertheless, in the case of a variable potency e_0, also normal earthquakes are promoted in the upper part of the TPE disk.

2.5. Modeling a TPE in a layered medium

According to equation 12, different elastic parameters of the embedding medium involve different magnitudes of the distributed single forces over the TPE boundaries, as they linearly depend on the incompressibility K. In the case of a TPE inclusion undergoing uniform changes of p and T, placed between two (or more) elastic layers, the proper distribution of single forces can be obtained considering the stack of two (or more) disks with equal potency e_0 but different K values (Figure 5 c). It is worth noting that due to the linear dependence of the single forces magnitude on both e_0 and K, the same distribution of single forces can be attained also assuming a variable e_0 and a uniform K (Figure 5 b) but, due to the elastic layering, the two cases are not equivalent (compare Figure 5 b and c).

3. Inversion of the deformation observed at the Campi Flegrei Caldera

The Caldera of Campi Flegrei, in Italy (Figure 6 a) was characterized by several episodes of volcanic activities since the last 47,000 years. In more recent times the Caldera activity has been mostly revealed by gas emission, fumaroles and by fast uplift episodes (bradyseism), interspersed with periods of subsidence (*e.g.* De Vivo, 2006; Di Vito et al., 2016; Gaeta et al., 2003). The last episode of major uplift occurred in 1982-1984 and reached a maximum of 1.8 m (*e.g.* Trasatti et al., 2011) in the city of Pozzuoli. At that time, the surface deformation data were acquired by leveling and electromagnetic distance measurement (EDM) with estimated errors generally greater than 1 cm, but still lower than the measured deformation. The locations of the EDM points, as well as the magnitude of uplift measured by leveling data in the campaign period 1980-1983, are reported in Figure 6 a. During recent years the caldera experienced several mini-uplift episodes of a maximum of few cm that could be measured with better precision thanks to more modern geodetic techniques, such as Interferometric Synthetic Aperture Radar (InSAR) and GPS (*e.g.* Pepe et al., 2019; Troise et al., 2007). Despite the alternation of phases with greater and lesser volcanic activity, the surface deformation pattern of the caldera has remained stable over time and is characterized by a nearly symmetrical shape with the center near the city of Pozzuoli. The volcanic unrest was always accompanied by

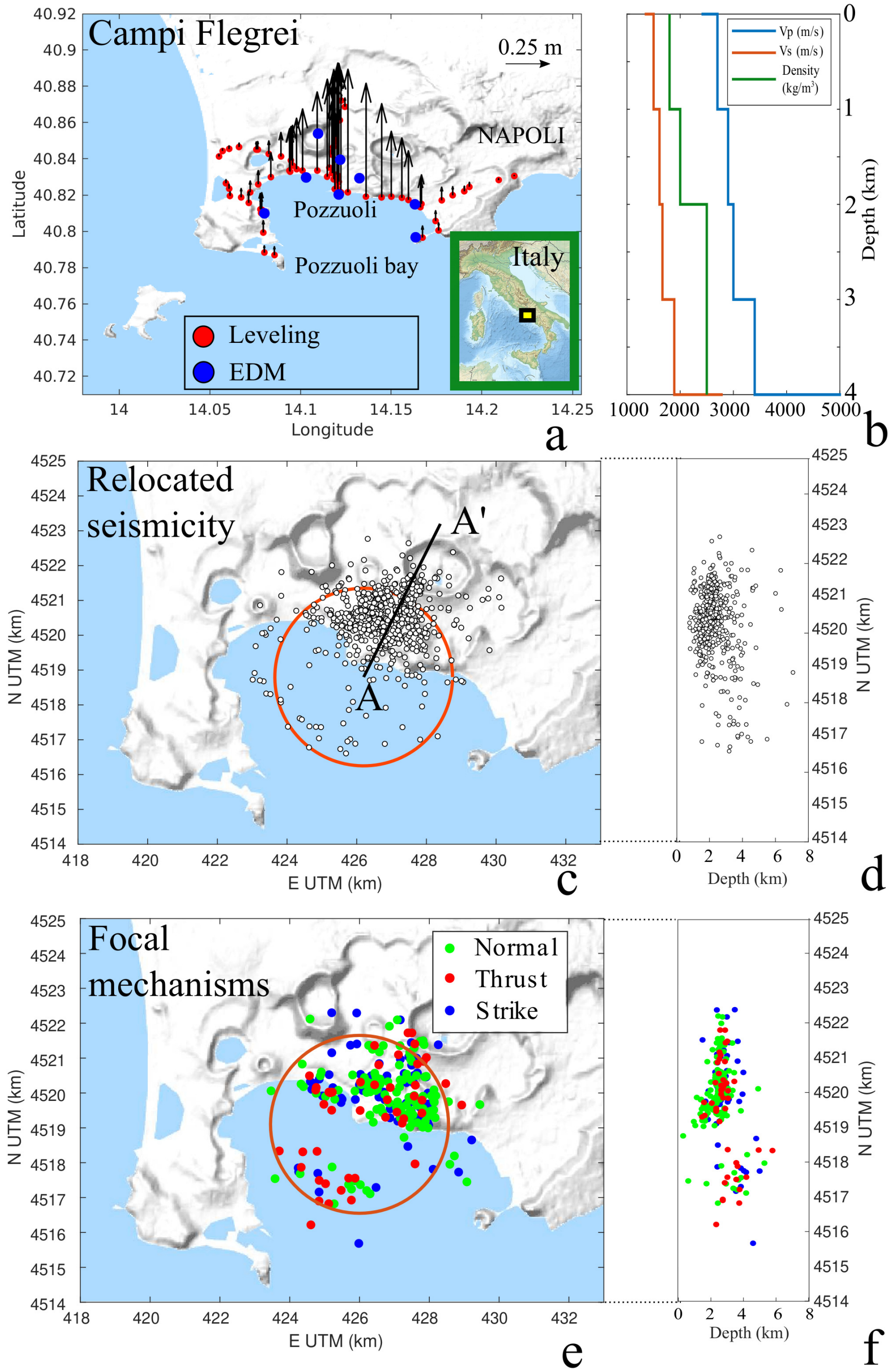

Figure 6: Map of the Campi Flegrei region (a). Blue and red circles respectively indicate the locations of EDM and leveling benchmarks. Black arrows represent the magnitude of uplift measured during the period June 1980-June 1983. Panel b shows the crustal model ($V_s = \sqrt{\mu/\rho}$, $V_p = \sqrt{(\lambda + 2\mu)/\rho}$ and ρ) used for the inversion in a layered half-space. The relocated seismicity (Calò and Tramelli, 2018) is shown as white circles both in map (c) and in a vertical cross section N-S oriented (d). Fault mechanisms, retrieved according to Frohlich (2001) from the seismic catalog of D'Auria et al. (2014), are shown both in map (e) and in a vertical cross section N-S oriented (f) with green, red and blue dots, representing normal, thrust and strike-slip mechanisms, respectively. The red circle in panels c and e represents the TPE inclusion boundary retrieved from the geodetic data inversion, assuming a layered half-space and a variable TPE inclusion potency e_0.

seismicity (Belardinelli et al., 2011), that occurs mostly above 3 km of depth (Figure 6) and it is characterized by a strong heterogeneity of focal mechanisms (*e.g.* D'Auria et al., 2014; Mantiloni et al., 2020). The up-to-date relocated seismicity (Calò and Tramelli, 2018) is shown in Figure 6 c and d. As focal mechanisms are not available in the Calò and Tramelli (2018) catalog, in Figure 6 e and f, we show the fault solution distribution retrieved (Frohlich, 2001) from a different seismic catalog (D'Auria et al., 2014) containing different locations and several different events. Hypocenters reported in the catalog by Calò and Tramelli (2018) were relocated according to their high resolution tomography and are considered more reliable.

Several deformation sources have been applied to model the big uplift occurred in 1982-1984, most of them are pressurized sources or cracks resembling magma volumes (*e.g.* Berrino et al., 1984; Amoruso et al., 2008; Bonafede et al., 1986; Trasatti et al., 2011), nevertheless several independent studies, based on seismic tomography and measured temperature profiles from drillings, exclude the presence of magma in the shallowest kilometers of the caldera (*e.g.* Judenherc and Zollo, 2004; Carlino et al., 2012). Accordingly, Mantiloni et al. (2020) proposed that the soil deformation occurring at Campi Flegrei is due to a combination of both a disk-shaped TPE inclusion and magmatic input.

Thanks to the numerical model implemented in the present work, we are able to invert the same geodetic data used by Mantiloni et al. (2020) and Trasatti et al. (2011) for a TPE inclusion located in a layered elastic half-space. The crustal model (Figure 6 b) is derived from average values of the 3D Vp/Vs tomography shown by Chiarabba and Moretti (2006) and Trasatti et al. (2011), which can be fairly approximated by horizontal layering. We also invert the data in the case of the homogeneous half-space, for comparison. In this case, the poro-elastic parameters of the TPE inclusion and surrounding medium are taken equal to the ones used by Mantiloni et al. (2020) (λ=4 GPa, μ= 6 GPa, $\alpha_s = 3 \cdot 10^{-5}\ K^{-1}$, $H = 10$ GPa). The inversion is performed by a Monte-Carlo sampling with a direct parameter search. Then, the best model is chosen as the one having the greater probability density distribution, PPD, (Sambridge, 1999; Mantiloni et al., 2020; Trasatti et al., 2011). Differently from Mantiloni et al. (2020), during the inversion: *i*) we allow the aspect$-$ratio d/a of the TPE disk to vary, exploring a wider parameter space, *ii*) we keep the thickness of the TPE inclusion fixed to 500 m. The latter choice is mainly due to the fact that there is a strong cross-talk between the TPE inclusion thickness d and potency e_0 being the displacement proportional to both parameters (*see* Figure 4, equation 2). Furthermore, to constrain a priori the thickness of the TPE source we take into account an information provided by Calò and Tramelli (2018) who found that the 1984 seismicity concentrates within a layer about 0.5 km thick at 2 km of depth, extending at least from the inland of the city of Pozzuoli to the coast. As mentioned in the introduction we interpret such layer as the TPE inclusion. It is worth noting that in the

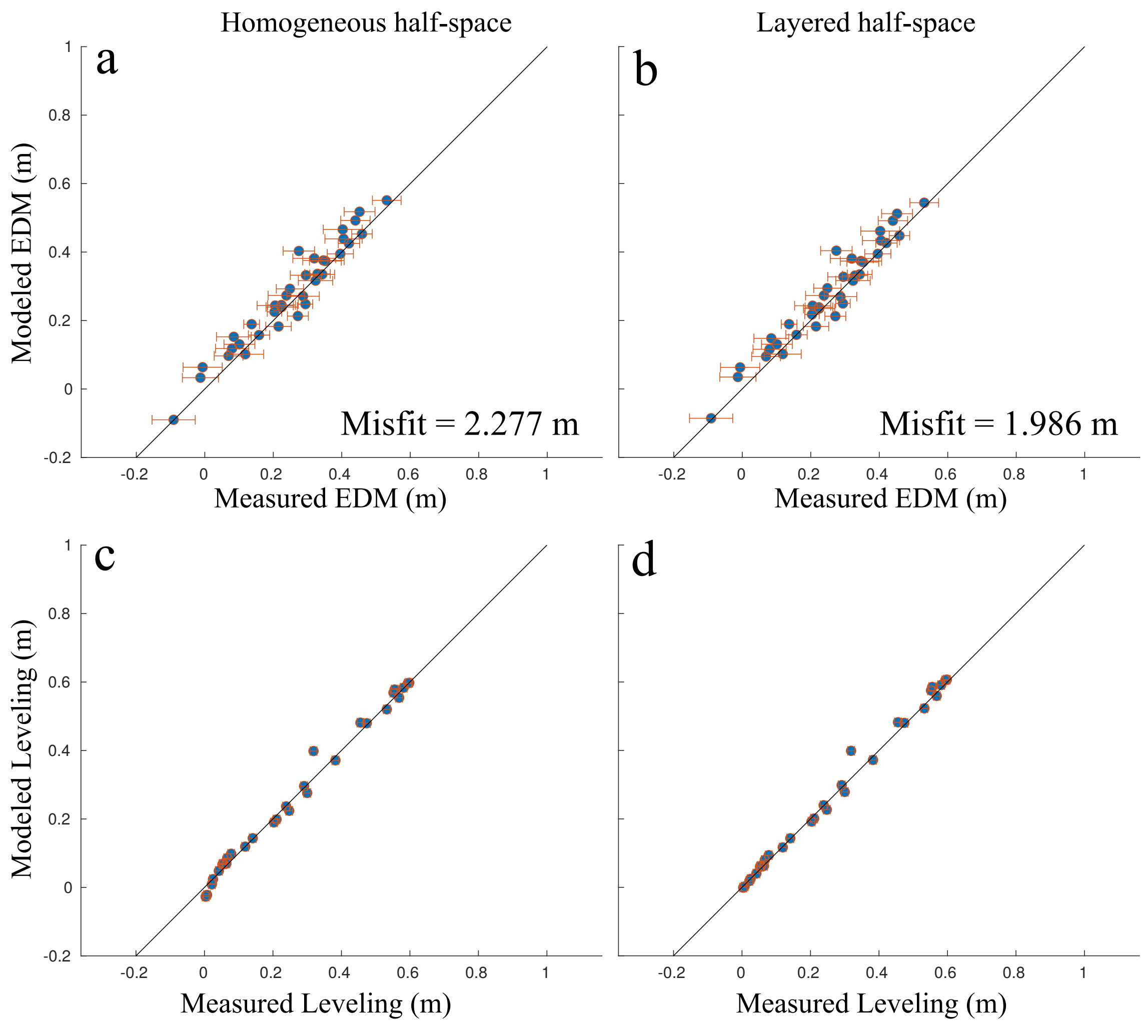

Figure 7: Plot of modeled (ordinate) and measured (abscissa) EDM (a, b) and Leveling (C, d) data obtained for the homogeneous (a, c) and layered (b, d) half-spaces. Orange bars represent measurement errors.

case of the layered medium, the inversion procedure may require to model the case of a TPE disk placed between two different elastic layers. The numerical solution of this case is attained considering the stack of two disks embedded in two different layers (similarly to Figure 5 c), with equal TPE inclusion potency e_0 but different K values (which depends on the elastic parameters of the crustal model). The comparison between modeled (inverted) and measured deformation is shown in Figure 7, while the resulting parameters are reported in Table 4.

The inversion performed in the layered half-space leads to a deeper TPE inclusion and a lower misfit, with respect to the homogeneous model, while the radius is almost the same and the TPE inclusion potency e_0 parameter does not change. It is worth noting that the order of magnitude of $e_0 = 10^{-3}$ (Table 4) can be easily obtained due to T=0 K and p=30 MPa or T=50 K and p=15 MPa (Table 2) if we employ values of Table 1. According to arguments presented in Section 2.1 such values of p and T are realistic for

Table 4: Parameters and misfit obtained by the inversion of geodetic data in a homogeneous and a layered medium with uniform e_0; and a layered medium with variable e_0. The latter inversion was performed keeping fixed the parameters a and h retrieved from the inversion in a layered medium and computing a second round inversion procedure for 4 different e_0 values at different depth intervals. In all cases $\alpha_s = 3 \cdot 10^{-5}$ K^{-1}, $H = 10$ GPa. For the homogeneous medium we used λ=4 GPa, μ= 6 GPa, while for the layered medium the elastic moduli are taken from the crustal model in Figure 6b. The thickness d is fixed to 500 m.

Half-space	a (m)	h (m)	TPE inclusion potency e_0	Total misfit (m)
Homogeneous	2525	1425	0.001	2.277
Layered	2550	1825	0.001	1.986
Layered (Variable e_0)	2550	1825	0.0001 ($1.575 < z < 1.7$ km) 0.0009 ($1.7 < z < 1.825$ km) 0.0019 ($1.825 < z < 2.0$ km) 0.0007 ($2.0 < z < 2.075$ km)	1.920

a TPE inclusion located at a few km depth. The case T=100 K and p=0 Pa (Table 2) can also explain a value $e_0 = 10^{-3}$, but it is unlike because temperature changes within the TPE inclusion are driven by fluid advection which depends on the pore pressure gradients. The resulting induced maximum shear stress is higher inside the TPE inclusion embedded in the homogeneous medium (Figure 8 b), at least above 2 km of depth, where the rigidity is low. In both cases, according to the Frohlich triangle (Frohlich, 2001), TPE sources promote normal earthquakes above and below them, while thrust mechanisms are favored inside them and laterally. Instead, strike-slip earthquakes are favoured in lateral sectors.

Displacement and stress components computed at the surface and on the median plane of the TPE inclusion retrieved by the inversion, in both homogeneous and layered medium are shown in Figure 9. As required by the inversion, displacements at the surface are very similar, while in the median plane they are slightly different. The stress field, instead, has a lower magnitude in the layered medium both at the surface and on the median plane of the TPE inclusion. Interestingly, even if at the surface both τ_{rr} and $\tau_{\phi\phi}$ are greater in the homogeneous medium, with respect to those of the layered medium, they decrease more rapidly moving away from the center of the TPE source (Figure 9 d).

Lastly we also study the effects of a depth dependent distribution of the TPE inclusion potency e_0. Similarly to the common approach followed in the inversion of geodetic data for slip distribution on fault planes (where the fault geometry is pre-determined assuming a uniform slip), we proceed as it follow. While keeping fixed the parameters retrieved form the inversion in the layered half-space, a and h, we performed a second round inversion for 4 different e_0 values at different depth intervals (Table 4 and Figure 10). With respect to the inversion performed in a layered medium with uniform e_0, the inversion with a variable e_0 leads to a slightly lower misfit, suggesting that the best fit of the data can be obtained assuming a low e_0 in the shallowest part of the inclusion. It is worth noting that in case of $e_0 = 0$ in the shallow part of the

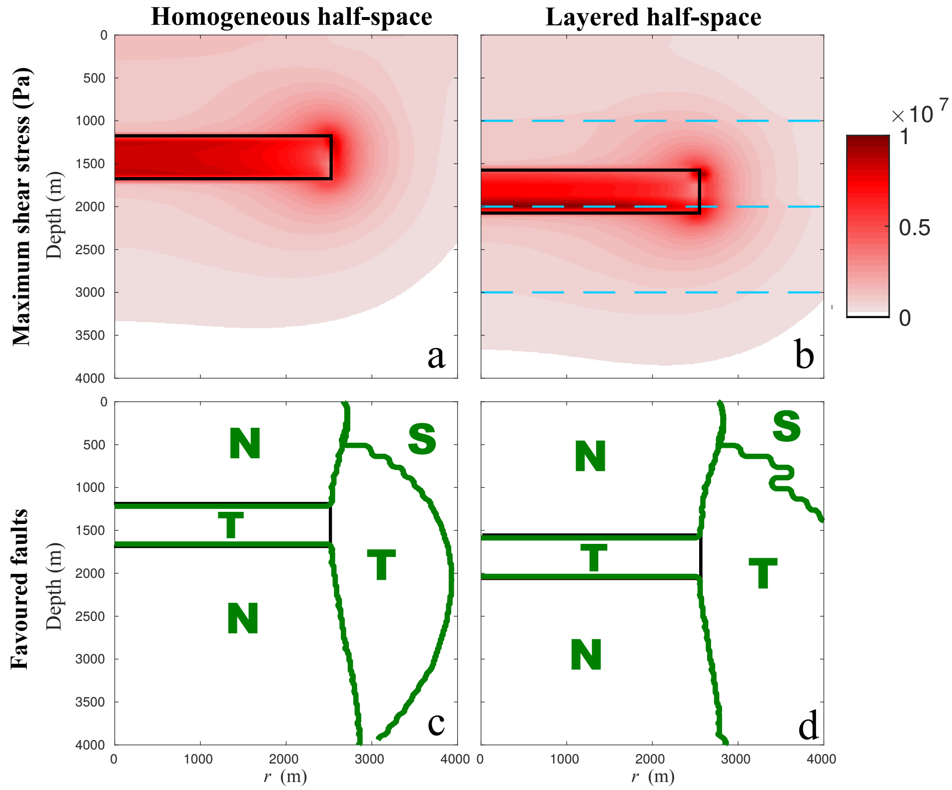

Figure 8: Maximum shear stress (Pa) induced by the TPE inclusion with uniform TPE inclusion potency found by inversion of geodetic data in the homogeneous (a) and heterogeneous (b) medium (model parameters reported in Table 4, first and second row). Black boxes represent the TPE inclusion boundaries. Cyan dashed lines represent the elastic layers. Green contours separates areas in which different earthquake mechanisms are favored (N=normal, S=strike-slip, T=thrust) in the homogeneous (c) and heterogeneous (d) medium.

inclusion, a TPE inclusion with a lower thickness can be sufficient to represent the data. We recall that according to section 2.1.1 results, $e_0 = 0$ is expected just at the top of the TPE inclusion.

4. Discussion

Previous works (Belardinelli et al., 2019; Mantiloni et al., 2020) showed that TPE inclusions, undergoing changes of pore pressure and temperature, represent an important kind of deformation sources in volcanic environments. With respect to magma-filled pressurized cavities the major advantage of TPE sources is that they allow large soil deformations even when the experimental evidences exclude the presence of molten magma at shallow depth. In the case of Campi Flegrei, temperature profiles measured by deep drillings are incompatible with magma at shallow (< 3 km) depth (Carlino et al., 2012; Trasatti et al., 2011). Another great advantage over pressurized sources, that are characterized by isotropic stress inside, is that a strong shear stress is generated within the TPE inclusion justifying the presence of earthquakes inside it. In the present work we extend the TPE inclusion models in order to: i) account for an arbitrary thickness of the inclusion; ii) insert a more realistic description of the embedding medium as a layered elastic half-space.

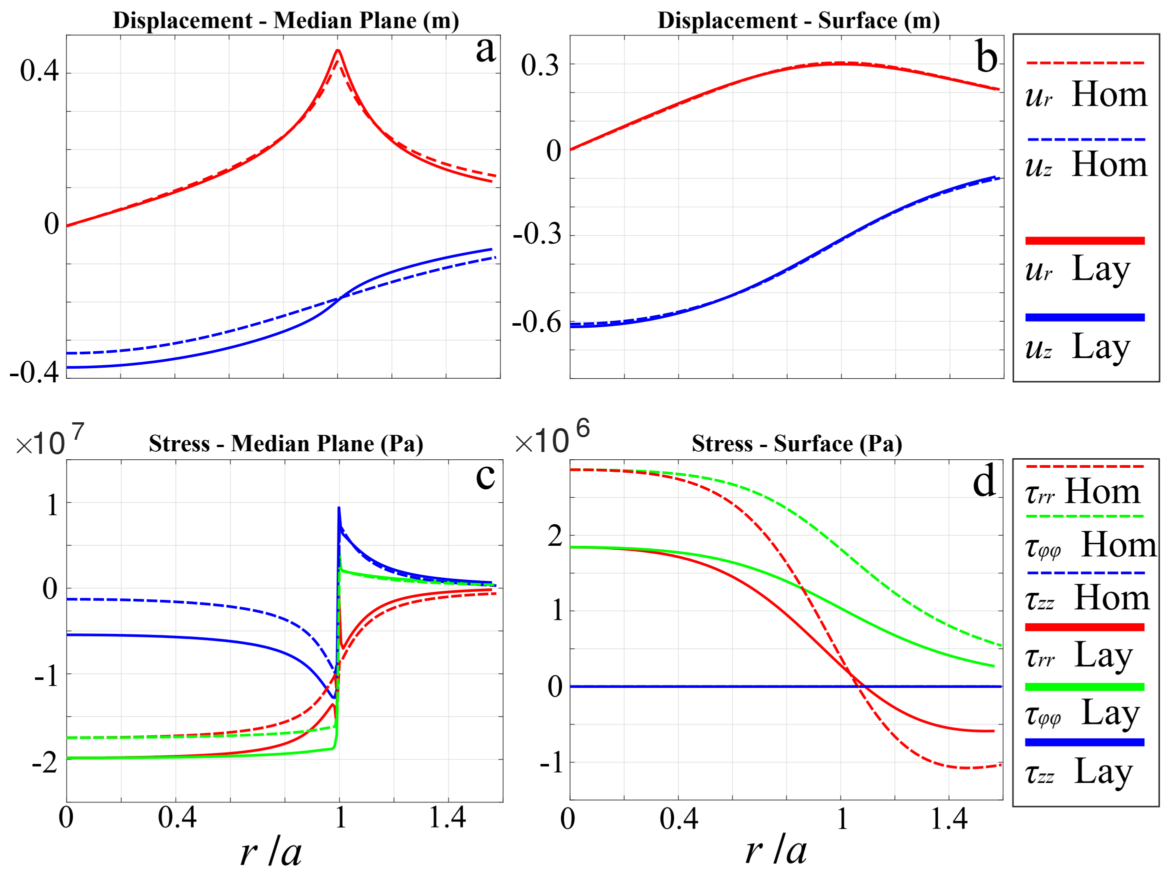

Figure 9: Displacement of the TPE inclusions retrieved from the inversion in a homogeneous (Hom) and layered (Lay) medium computed on the median plane $z = h$ (a) and at the surface $z = 0$ (b). Stress of the TPE inclusions retrieved from the inversion in a homogeneous (Hom) and layered (Lay) medium computed on the median plane (c) and at the surface (d). Model parameters are reported in Table 4, first and second row.

Considering a TPE source with a finite thickness allows reproducing the expected distribution of its effects within internal region and extends its applicability to other environments (*e.g.* geothermal reservoirs, Volpi et al., 2018), in which the assumption of a thin inclusion is unrealistic. The introduction of a layered medium is also important, especially when inverting geodetic data, since the elastic layering significantly affects the results (*e.g.* Trasatti et al., 2011; Nespoli et al., 2017).

4.1. Modeling thick TPE inclusions

The model used in the present work is obtained through a modified version of the EDGRN/EDCMP code (Wang et al., 2003), suitably adapted to represent deformation and stress induced by a distribution of single forces. Results indicate that a thick disk ($d/a \leq 1$) inclusion can be modeled as a superposition of thin piled-up disks. Accordingly, semi-analytical solutions provided by Mantiloni et al. (2020) can be used to represent thick TPE sources, provided that they are discretized with a sufficient high number of sub-disks

(Figure 3 b, c). The case of a very thick TPE inclusion ($d/a > 1$, Figure 3 d) instead, requires a careful implementation when using semi-analytical solutions, as discussed in section 1. Our model indicates that shear stresses inside the TPE disks are reduced by increasing the inclusion thickness and when the aspect ratio is $d/a = 2$ the stress field is nearly isotropic, resembling magma-filled sources (*e.g.* Yang et al., 1988; Mogi, 1958).

4.2. Variable TPE inclusion potency

On the basis of results obtained in 2.1, a uniform TPE inclusion potency may represent the case of a large change of temperature due to input of hot fluids ($\alpha_S \Delta T >> \Delta p/H$) when the temperature front has already reached the top of the inclusion, that is for $t \sim t_T$ (Figure 2*a*). The condition of a variable TPE inclusion potency (*e.g.* Figure 5*b*) can be useful to represent depth dependent gradients (Zencher et al., 2006; Stefánsson et al., 2011). The latter can be established when fluids rising upward from a deep magmatic source enter from the bottom of the TPE disk and progressively flow into the upper part of the inclusion. According to section 2.1.1) depth dependent TPE inclusion potency are established *i)* for large changes of temperature before the thermal front reaches the top the inclusion ($t < t_T$, Figure 2*a*), or *ii)* when the effects of pore pressure changes prevail on the ones due to temperature changes ($\alpha_S \Delta T \sim \Delta p/H$, Figure 2*b*).

4.3. Effects of a TPE inclusion at Campi Flegrei

Different independent studies show that there was heterogeneity of focal mechanisms close to each other during 1982-1984 Campi Flegrei unrest (*e.g.* D'Auria et al., 2014; Zuppetta and Sava, 1991; Orsi et al., 1999). This was also envisaged in other volcanic regions (*e.g.* Ekstrom, 1994; Nettles and Ekstrom, 1998) with the unexpected presence of thrust mechanisms. Depth dependent TPE inclusion potency can provide a solution to the heterogeneity of focal mechanisms inside the same source of deformation. In fact in the case of a depth dependent e_0 (Figure 5 b), both thrust and normal earthquakes can be favored, at least in the upper part of the TPE disk.

For the big uplift occurred in 1982-1984 unrest in the caldera of Campi Flegrei, we also invert available geodetic data assuming the TPE source located within either a homogeneous or a heterogeneous poroelastic half-space. Taking into account vertical heterogeneities is very important to retrieve correct source parameters at Campi Flegrei (*e.g.* Crescentini and Amoruso, 2007). 3-D crustal models derived from seismic tomography with good enough resolution can even do better (*e.g.* Manconi et al., 2010), because they allow for a more realistic forward modeling of the deformation pattern. Bayesian-type inversions accounting for a 3-D heterogeneous medium are however very demanding in terms of computation resources and time as they ask to use finite elements methods (*e.g.* Trasatti et al., 2011). The modified EDGRN/EDCMP application is restricted to a 1-D crustal structure, but allows for a quick and semi-analytic representation of the elastic deformation (Wang et al., 2003). Elastic layering leads to a (400 m) deeper TPE inclusion (Table 3 and Figure 8). This behavior was also envisaged by Trasatti et al. (2011) for another kind of deformation source and by Nespoli et al. (2017) for a different dataset. Figure 9 shows that even if both inversion solutions reproduce a similar displacement, the stress obtained in the case of a layered medium has a lower magnitude. The TPE inclusion obtained using the more realistic layered medium is located at 1825 m of depth and it has a radius of 2550 m. Both the geometry and location are in good agreement with the seismic layer regulating the ascent of fluid flow found by Calò and Tramelli (2018), (Figure 9). The concentration of earthquakes around and within the TPE source domain (Figure 10) is a strong evidence of the importance of this kind of deformation source in the complex system of the Campi Flegrei caldera. The inversion performed in a layered medium leads to an improved agreement with data (Figure 7) with a significantly lower misfit (1.986 m, Table 3) with respect to the case of a homogeneous medium (2.277 m) and Mantiloni et al. (2020), with a misfit of 2.904 m. The misfit is even slightly lower (1.920, Table 4) if a depth dependent distribution of e_0 is assumed inside the inclusion.

In the 1982-84 unrest episode at Campi Flegrei, the inversion of geodetic data for e_0 (Table 4) as a function of depth shows that the TPE inclusion potency has a relative maximum near 2 km depth, decreasing sharply both below and above. Even if the misfit decrease with respect to the uniform case is relatively small, this result is in good agreement with the high permeability solution presented in Section 2.1. The low value of TPE inclusion potency retrieved below 2 km can be explained by smaller temperature increments there, with respect to initial higher temperature in proximity of the exsolving reservoir. The maximum value of TPE inclusion potency is estimated as $e_0 = 0.002$ (Table 4) and is in agreement with acceptable values of Δp and ΔT (Table 2). Nonetheless, in order to explain the uplift of 1.8 m observed in November 1984 a three times larger TPE inclusion potency would be necessary, *i.e.* up to $e_0 \sim 0.006$. While such a high value is consistent with quite large Δp and ΔT (*e.g.* $\Delta p = 30$ MPa and $\Delta T = 500$ K), we believe that a significant fraction of the observed deformation may be ascribed to the inflation of the underlying magma reservoir.

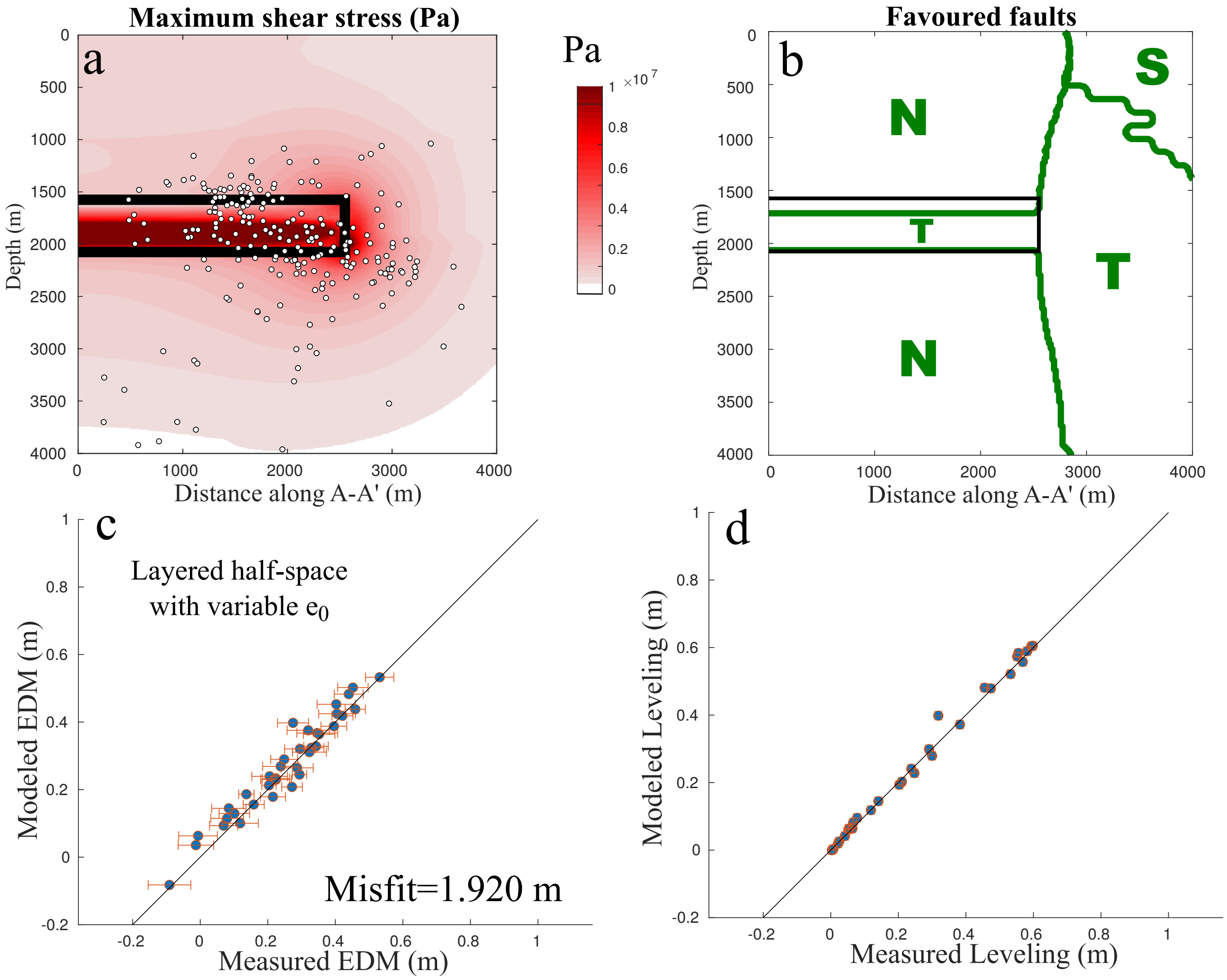

Figure 10: (a) Maximum shear stress induced by the TPE inclusion embedded in the layered medium (color) plotted together with the relocated seismicity (Calò and Tramelli, 2018) projected onto the vertical slice A-A' (Figure 6) within $\pm$ 0.5 km. Black lines represent the TPE inclusion boundaries. (b) Green contours separates areas in which different earthquake mechanisms are favored (N=normal, S=strike-slip, T=thrust). Plot of modeled (ordinate) and measured (abscissa) EDM (c) and Leveling (d) data obtained for a TPE inclusion with variable potency e_0 (determined from inversion of geodetic data for assumed values of d, a and h, see Table 4 third row). Orange bars represent measurement errors.

It is worth noting that even for the high permeability case, the thermal advection front needs a time $t = t_T \simeq 3$ yr (see subsection 2.1.1) to reach the top of the TPE inclusion, in intriguing similarity with the uplift duration at Campi Flegrei. The geodetic data here inverted reach only June 1983, covering a 1.5 year of uplift, that is about half of t_T. Then it is reasonable that at June 1983 the thermal advection front had not reached the top of the inclusion yet. This is consistent with the fact that e_0 distribution obtained by inversion of geodetic data resembles the one of a transient configuration $0 < t < t_T$ (Figure 2*b*).

5. Conclusions

The numerical approach used in the present work produces a significant step forward for the modeling of the displacement and stress produced by thermo-poro-elastic inclusions. With respect to previous semi-analytical models, our approach allows a greater versatility in the choice of the source geometry and it accounts for a greater realism of the elastic medium embedding the inclusion. Thanks to our model we were able to study what happens inside the TPE inclusion in the case of non-uniformity of the thermo-poro-elastic parameters as derived from a (T, p) propagation model. Starting from these results, future developments could be focused on the modeling of dynamic processes that can occur inside and outside the source, as a consequence of the movement of hydrothermal fluids. It would be interesting to study how a decrease of pore pressure within TPE inclusions could explain the subsidence phases which follow the unrest periods. Furthermore, it could be also interesting to study the effect of different geometries of TPE inclusions, since the numerical model we have implemented can also represent complex, non symmetrical geometries.

6. Acknowledgments

We thank Marco Caló, Anna Tramelli and Luca D'Auria for sharing seismic catalogs and Elisa Trasatti for sharing the crustal model. We thank the reviewers for constructive comments. Maps of Figure 6 has been realized with the MATLAB function, https://github.com/zoharby/plot_google_map , using Google Maps API.

References

Aki, K. and Richards, P. (2002). *Quantitative Seismology.* University Science Books.

Amoruso, A., Crescentini, L., and Berrino, G. (2008). Simultaneous inversion of deformation and gravity changes in a horizontally layered half-space: evidences for magma intrusion during the 1982–1984 unrest at campi flegrei caldera (italy). *Earth and Planetary Science Letters*, 272(1-2):181–188.

Backus, G. and Mulcahy, M. (1976). Moment tensors and other phenomenological descriptions of seismic sourcesi. continuous displacements. *Geophysical Journal of the Royal Astronomical Society*, 46(2):341–361.

Bejan, A. (1984). *Convection Heat Transfer.* Wiley.

Belardinelli, M., Bizzarri, A., Berrino, G., and Ricciardi, G. (2011). A model for seismicity rates observed during the 1982-1984 unrest at campi flegrei caldera (italy). *Earth and Planetary Science Letters*, 302(3):287–298.

Belardinelli, M., Bonafede, M., and Nespoli, M. (2019). Stress heterogeneities and failure mechanisms induced by temperature and pore-pressure increase in volcanic regions. *Earth and Planetary Science Letters*, 525:115765.

Berrino, G., Corrado, G., Luongo, G., and Toro, B. (1984). Ground deformation and gravity changes accompanying the 1982 pozzuoli uplift. *Bulletin volcanologique*, 47(2):187–200.

Bonafede, M., Dragoni, M., and Quareni, F. (1986). Displacement and stress fields produced by a centre of dilation and by a pressure source in a viscoelastic half-space: Application to the study of ground deformation and seismic activity at campi flegrei, italy. *Geophysical Journal of the Royal Astronomical Society*, 87(2):455–485.

Bonafede, M. and Ferrari, C. (2009). Analytical models of deformation and residual gravity changes due to a mogi source in a viscoelastic medium. *Tectonophysics*, 471(1-2):4–13.

Calò, M. and Tramelli, A. (2018). Anatomy of the campi flegrei caldera using enhanced seismic tomography models. *Scientific Reports*, 8(16254).

Carlino, S., Somma, R., Troise, C., and Natale, G. D. (2012). The geothermal exploration of campanian volcanoes: Historical review and future development. *Renewable and Sustainable Energy Reviews*, 16(1):1004 – 1030.

Chiarabba, C. and Moretti, M. (2006). An insight into the unrest phenomena at the campi flegrei caldera from vp and vp/vs tomography. *Terra Nova*, 18(6):373–379.

Crescentini, L. and Amoruso, A. (2007). Effects of crustal layering on the inversion of deformation and gravity data in volcanic areas: An application to the campi flegrei caldera, italy. *Geophysical Research Letters*, 34(9).

D'Auria, L., Giudicepietro, F., Aquino, I., Borriello, G., Del Gaudio, C., Lo Bascio, D., Martini, M., Ricciardi, G. P., Ricciolino, P., and Ricco, C. (2011). Repeated fluid-transfer episodes as a mechanism for the recent dynamics of campi flegrei caldera (1989-2010). *Journal of Geophysical Research: Solid Earth*, 116(B4).

D'Auria, L., Massa, B., Cristiano, E., Gaudio, C. D., Giudicepietro, F., Ricciardi, G., and Ricco, C. (2014). Retrieving the stress field within the campi flegrei caldera (southern italy) through an integrated geodetical and seismological approach. *Pure and Applied Geophysics*, 172(11):3247–3263.

De Siena, L., Del Pezzo, E., and Bianco, F. (2010). Seismic attenuation imaging of campi flegrei: Evidence of gas reservoirs, hydrothermal basins, and feeding systems. *Journal of Geophysical Research: Solid Earth*, 115(B9).

De Vivo, B. (2006). *Volcanism in the Campania Plain: Vesuvius, Campi Flegrei and Ignimbrites*, volume 9. Elsevier.

Di Vito, M. A., Acocella, V., Aiello, G., Barra, D., Battaglia, M., Carandente, A., Gaudio, C. D., Vita, S. D., Ricciardi, G. P., Ricco, C., et al. (2016). Magma transfer at campi flegrei caldera (italy) before the 1538 ad eruption. *Scientific reports*, 6:32245.

Ekstrom, G. (1994). Anomalous earthquakes on volcano ring-fault structures. *Earth and Planetary Science Letters*, 128(3):707 – 712.

Eshelby, J. D. (1957). The determination of the elastic field of an ellipsoidal inclusion, and related problems. *Proc. R. Soc. Lond. A*, 241(1226):376–396.

Fialko, Y., Khazan, Y., and Simons, M. (2001). Deformation due to a pressurized horizontal circular crack in an elastic half-space, with applications to volcano geodesy. *Geophysical Journal International*, 146(1):181–190.

Frohlich, C. (2001). Display and quantitative assessment of distributions of earthquake focal mechanisms. *Geophysical Journal International*, 144(2):300–308.

Gaeta, F. S., Peluso, F., Arienzo, I., Castagnolo, D., Natale, G. D., Milano, G., Albanese, C., and Mita, D. G. (2003). A physical appraisal of a new aspect of bradyseism: The miniuplifts. *Journal of Geophysical Research: Solid Earth*, 108(B8).

Gudmundsson, A. (2020). *Volcanic Earthquakes*, pages 179–223. Cambridge University Press.

Judenherc, S. and Zollo, A. (2004). The bay of naples (southern italy): Constraints on the volcanic structures inferred from a dense seismic survey. *Journal of Geophysical Research: Solid Earth*, 109(B10).

Lima, A., Vivo, B. D., Spera, F. J., Bodnar, R. J., Milia, A., Nunziata, C., Belkin, H. E., and Cannatelli, C. (2009). Thermodynamic model for uplift and deflation episodes (bradyseism) associated with magmatic–hydrothermal activity at the campi flegrei (italy). *Earth-Science Reviews*, 97(1-4):44–58.

Macedonio, G., Giudicepietro, F., D'auria, L., and Martini, M. (2014). Sill intrusion as a source mechanism of unrest at volcanic calderas. *Journal of Geophysical Research: Solid Earth*, 119(5):3986–4000.

Manconi, A., Walter, T. R., Manzo, M., Zeni, G., Tizzani, P., Sansosti, E., and Lanari, R. (2010). On the effects of 3-d mechanical heterogeneities at campi flegrei caldera, southern italy. *Journal of Geophysical Research: Solid Earth*, 115(B8).

Mantiloni, L., Nespoli, M., Belardinelli, M. E., and Bonafede, M. (2020). Deformation and stress in hydrothermal regions: The case of a disk-shaped inclusion in a half-space. *Journal of Volcanology and Geothermal Research*, 403:107011.

McKee, C., Mori, J., and Talai, B. (1989). Microgravity changes and ground deformation at rabaul caldera, 1973–1985. In Latter, J. H., editor, *Volcanic Hazards*, pages 399–428, Berlin, Heidelberg. Springer Berlin Heidelberg.

McTigue, D. F. (1986). Thermoelastic response of fluid-saturated porous rock. *Journal of Geophysical Research: Solid Earth*, 91(B9):9533–9542.

McTigue, D. F. (1987). Elastic stress and deformation near a finite spherical magma body: Resolution of the point source paradox. *Journal of Geophysical Research: Solid Earth*, 92(B12):12931–12940.

Mindlin, R. D. (1936). Force at a point in the interior of a semi-infinite solid. *Physics*, 7(5):195–202.

Mogi, K. (1958). Relations between the eruptions of various volcanoes and the deformations of the ground surfaces around them. *Earthq Res Inst*, 36:99–134.

Nespoli, M., Belardinelli, M., Gualandi, A., Serpelloni, E., and Bonafede, M. (2018). Poroelasticity and fluid flow modeling for the 2012 emilia-romagna earthquakes: Hints from gps and insar data. *Geofluids*, 2018. cited By 7.

Nespoli, M., Belardinelli, M. E., Anderlini, L., Bonafede, M., Pezzo, G., Todesco, M., and Rinaldi, A. P.

(2017). Effects of layered crust on the coseismic slip inversion and related cff variations: Hints from the 2012 emilia romagna earthquake. *Physics of the Earth and Planetary Interiors*, 273:23 – 35.

Nettles, M. and Ekstrom, G. (1998). Faulting mechanism of anomalous earthquakes near brdarbunga volcano, iceland. *Journal of Geophysical Research: Solid Earth*, 103(B8):17973–17983.

Okada, Y. (1985). Surface deformation due to shear and tensile faults in a half-space. *Bulletin of the Seismological Society of America*, 75(4):1135–1154.

Okada, Y. (1992). Internal deformation due to shear and tensile faults in a half-space. *Bulletin of the Seismological Society of America*, 82(2):1018–1040.

Orsi, G., Civetta, L., Del Gaudio, C., de Vita, S., Di Vito, M., Isaia, R., Petrazzuoli, S., Ricciardi, G., and Ricco, C. (1999). Short-term ground deformations and seismicity in the resurgent campi flegrei caldera (italy): an example of active block-resurgence in a densely populated area. *Journal of Volcanology and Geothermal Research*, 91(2):415–451.

Pepe, S., De Siena, L., Barone, A., Castaldo, R., D'Auria, L., Manzo, M., Casu, F., Fedi, M., Lanari, R., Bianco, F., and Tizzani, P. (2019). Volcanic structures investigation through sar and seismic interferometric methods: The 20112013 campi flegrei unrest episode. *Remote Sensing of Environment*, 234:111440.

Rice, J. R. and Cleary, M. P. (1976). Some basic stress diffusion solutions for fluid-saturated elastic porous media with compressible constituents. *Reviews of Geophysics*, 14(2):227–241.

Rinaldi, A., Todesco, M., and Bonafede, M. (2010). Hydrothermal instability and ground displacement at the campi flegrei caldera. *Physics of the Earth and Planetary Interiors*, 178(3):155 – 161.

Sambridge, M. (1999). Geophysical inversion with a neighbourhood algorithm-II. Appraising the ensemble. *Geophysical Journal International*, 138(3):727–746.

Stefánsson, R., Bonafede, M., and Gudmundsson, G. B. (2011). Earthquake-Prediction Research and the Earthquakes of 2000 in the South Iceland Seismic Zone. *Bulletin of the Seismological Society of America*, 101(4):1590–1617.

Todesco, M., Rinaldi, A. P., and Bonafede, M. (2010). Modeling of unrest signals in heterogeneous hydrothermal systems. *Journal of Geophysical Research: Solid Earth*, 115(B9).

Trasatti, E., Bonafede, M., Ferrari, C., Giunchi, C., and Berrino, G. (2011). On deformation sources in volcanic areas: modeling the campi flegrei (italy) 1982–84 unrest. *Earth and Planetary Science Letters*, 306(3-4):175–185.

Troise, C., De Natale, G., Pingue, F., Obrizzo, F., De Martino, P., Tammaro, U., and Boschi, E. (2007). Renewed ground uplift at campi flegrei caldera (italy): New insight on magmatic processes and forecast. *Geophysical Research Letters*, 34(3).

Volpi, G., Magri, F., Colucci, F., Fisher, T., De Caro, M., and Crosta, G. (2018). Modeling highly buoyant flows in the castel giorgio: Torre alfina deep geothermal reservoir. *Geofluids*, 2018(3818629):19.

Wang, H. F. (2017). *Theory of linear poroelasticity with applications to geomechanics and hydrogeology*. Princeton University Press.

Wang, R., Martin, F. L., and Roth, F. (2003). Computation of deformation induced by earthquakes in a multi-layered elastic crustfortran programs edgrn/edcmp. *Computers and Geosciences*, 29(2):195 – 207.

Yang, X.-M., Davis, P. M., and Dieterich, J. H. (1988). Deformation from inflation of a dipping finite prolate spheroid in an elastic half-space as a model for volcanic stressing. *Journal of Geophysical Research: Solid Earth*, 93(B5):4249–4257.

Zencher, F., Bonafede, M., and Stefansson, R. (2006). Near-lithostatic pore pressure at seismogenic depths: a thermoporoelastic model. *Geophysical Journal International*, 166(3):1318–1334.

Zuppetta, A. and Sava, A. (1991). Stress pattern at campi flegrei from focal mechanisms of the 19821984 earthquakes (southern italy). *Journal of Volcanology and Geothermal Research*, 48(1):127–137.